Impact of Defects in Powder Feedstock Materials on Microstructure of 304L and 316L Stainless Steel Produced by Additive Manufacturing

BENJAMIN M. MORROW, THOMAS J. LIENERT, CAMERON M. KNAPP,
JACOB O. SUTTON, MICHAEL J. BRAND, ROBIN M. PACHECO,
VERONICA LIVESCU, JOHN S. CARPENTER, and GEORGE T. GRAY III

Recent work in both 304L and 316L stainless steel produced by additive manufacturing (AM) has shown that in addition to the unique, characteristic microstructures formed during the process, a fine dispersion of sub-micron particles, with a chemistry different from either the powder feedstock or the expected final material, are evident in the final microstructure. Such fine-scale features can only be resolved using transmission electron microscopy (TEM) or similar techniques. The present work uses electron microscopy to study both the initial powder feedstock and microstructures in final AM parts. Special attention is paid to the chemistry and origin of these nanoscale particles in several different metal alloys, and their impact on the final build. Comparisons to traditional, wrought material will be made.

I. INTRODUCTION

ADDITIVE manufacturing (AM) is an emerging technique to create near-net shape parts in complex geometries for a variety of applications.[1,2] Several commercial methods are available to produce parts from a wide variety of materials, including structural metals, such as stainless steels. Though there are many different types of AM processes, most are linked by the common goal of localized melting and relatively rapid solidification of precursor material (typically 10^4 to 10^6 K/s) to create solid volumes of fused material in prescribed shapes. Each technique then has some unique processing parameters (*i.e.*, method of powder distribution, powder size, laser power, and travel speed and pattern) which may weigh differently on the final part.

Metal powder is a commonly used feedstock for processes such as directed energy deposition (*i.e.*, the Optomec system used in this work), and powder bed fusion (*i.e.*, the EOS system presented here).[3] Much of the current research efforts in the field of AM are devoted to understanding processing parameters and their effect on materials properties and, ultimately, part performance.[3–9] Relatively fewer studies characterize the initial powder feedstocks and effects they might have on the final parts. Those that do study feedstock sometimes note the size distribution and morphology of the feedstock as an important parameter in the AM process (such as Reference 10), or focus on changes as a function of powder reuse (such as Reference 11). There are a few studies following internal porosity from powder to final part, such as the works of Ng *et al.*,[12] and Cunningham *et al.*[13–15] Even so, the effects of defects present in virgin powder, especially with regard to powder chemistry, and their effect on the final microstructure remain largely unstudied.

The present work examines AM powder feedstock particles designed for two different AM processes. AM parts were built using each process, and the final microstructures were characterized. Selected parts were heat treated after the build process to examine changes in microstructure due to temperature. During post-mortem investigation of AM parts, a fine dispersion of sub-micron particles was observed in the microstructure. Such particles were strongly correlated with ductile dimples on fracture surfaces. Post-mortem TEM of as-built and heat-treated specimens was used to characterize the particles. The general composition was measured, and it was revealed that the particle sizes and distributions were not greatly affected by post-build heat-treatment. Furthermore, these particles are not present in traditionally manufactured, wrought material. TEM studies are rarely performed on AM

BENJAMIN M. MORROW, THOMAS J. LIENERT, CAMERON M. KNAPP, JACOB O. SUTTON, MICHAEL J. BRAND, ROBIN M. PACHECO, VERONICA LIVESCU, JOHN S. CARPENTER, and GEORGE T. GRAY III are with the Los Alamos National Laboratory, P.O. Box 1663, MS G755, Los Alamos, NM 87545. Contact e-mail: morrow@lanl.gov

materials, so these sub-micron microstructural features are generally unreported in literature. In order to determine the origin of these particles, a small study of the powder feedstock was performed. Investigation of the 304L and 316L stainless steel powders used to create the AM parts revealed a fine dispersion of particles on the surface of the powders. Chemical analysis of surface particles revealed compositions drastically different than the parent alloy material. Additionally, a series of defects internal to the powder granules (porosity) was observed. Such features may persist throughout the build process and remain throughout the microstructure in built parts, and therefore are an important consideration to the AM lifecycle, especially for quality assurance and part/process qualification and certification purposes. Additionally, these observations may provide insights into important considerations for defect characterization with regard to powder reuse.

II. EXPERIMENTAL PROCEDURES

AM parts were built using both the Optomec Laser Engineered Net Shape (LENS) MR-7 laser additive manufacturing system (representing directed energy deposition), and an Electro-Optical Systems (EOS) M280 laser powder bed system (representing powder bed fusion). Powder feedstock was procured from Carpenter Powder Products in two different alloys: 304L and 316L stainless steel. Additionally, two separate lots of 304L powder were procured, representing both a commercial off-the-shelf (COTS) product, and a pedigreed powder (ADET) with a lower sulfur content. Thus, three different powder chemistries were explored in this work. The compositions of the major alloying elements in each powder are shown in Table I, along with nominal compositions for each alloy. Size distribution was selected to be compatible with either the LENS or the EOS systems, as appropriate, as each system has a different manufacturer-suggested particle size as a result of their respective build mechanics. The LENS 316L powder particle size was constrained between 53 and 180 μm by standard sieving, while the LENS 304L powder was between 44 and 106 μm. The EOS 304L powder was finer, between 15 and 45 μm.

AM parts were built using the same settings from previous work; Complete details of the build parameters can be found elsewhere.[4,5] Briefly, the 316L parts were built using the LENS, as solid cylinders, 2.5 cm in diameter and 3.3 cm tall, deposited onto a 0.95-cm-thick 304L plate substrate. A 1070 nm Yb-fiber laser at 380W was used to melt the powder, which was fed at a constant rate of 6.26 g/min. Laser focal length was 160.4 mm, and the focus condition was set such that the minimum waist of the focused beam was ~3.8 mm below the surface. Each layer was patterned at 1.12 cm/s, with a 90° rotation of the hatching between layers. An argon atmosphere was used to minimize oxygen uptake. After fabrication, the 304L substrate was machined away, and the cylinders were sectioned using electrical discharge machining (EDM). Sections of one cylinder were heat treated at 1060 °C for one hour in vacuum to recrystallize the microstructure and cooled to room temperature in 2.5 minutes by rapid gas quenching using argon.

The 304L material was built as vertical plate material using both the LENS and EOS systems. For the LENS, specimens were fabricated on a 304L baseplate in the vertical direction. Laser power was 800W. Each layer was patterned at 1.693 cm/s with a 90° rotation of the hatching between layers. An argon atmosphere was used to minimize oxygen uptake. For the EOS, specimens were fabricated on a 50.5-mm-thick 304L baseplate with a vertical build direction using the EOS-developed PH-1 20 μm (layer height) setting. Aside from layer height (20 μm), most of the build parameters were obscured by the proprietary software.

Several flat dogbone tensile specimens were prepared from the 316L material and tested to failure to observe the behavior at the fracture surfaces. The tensile axis was parallel to the build direction, with a 10.16 mm gauge length, 2.69 mm gauge width, and 3.175 mm thickness. Fractography was performed on the fracture surfaces as tested, without additional preparation.

Powder samples were prepared for SEM by pouring powder onto carbon tape fixed to an aluminum stub and tapping the side of the stub to remove any loose, excess powder. An FEI Inspect scanning electron microscope (SEM) was used to image fracture surfaces and powder samples. To obtain cross sections of each powder, a layer of powder was encased in epoxy and prepared metallographically by standard grinding and polishing techniques. A Zeiss Axio Imager M2m light optical microscope was used to image powder cross sections. Samples for general metallography of the post-build AM microstructures were sectioned and prepared using standard metallographic techniques to enable analysis in an electron microscope. An FEI XL30 SEM equipped with an TSL/EDAX electron backscatter diffraction (EBSD) system was used to measure grain orientations. Each scan was cleaned with a single iteration of the Neighbor Confidence Index (CI) Correlation in the TSL/EDAX software, with a minimum CI of 0.05.

Table I.   Chemical Compositions of Powder Feedstocks and Nominal Compositions for Each Alloy (Weight Percent)

Grade	Cr	Ni	Mn	Mo	Si	C	S	P	N	O	Fe
304L nominal	18 to 20	8 to 12	< 2	—	< 0.75	< 0.03	< 0.03	< 0.045	< 0.10	—	balance
304L powder—COTS	18.5	9.8	1.5	0.0	0.77	0.020	0.009	0.008	0.08	0.023	balance
304L powder—ADET	18.5	9.8	1.5	0.0	0.53	0.015	0.003	0.012	0.05	0.019	balance
316L nominal	16 to 18	10 to 14	< 2	2 to 3	< 0.75	< 0.03	< 0.03	< 0.045	< 0.10	—	balance
316L powder	20.70	11.40	1.32	2.45	0.5	0.02	0.01	0.02	0.09	—	balance

Conventional foils for analysis using a transmission electron microscope (TEM) were prepared by thinning sectioned material to ~150 μm using standard metallographic techniques and using a specialized punch to create discs with 3mm diameters without damaging the center of the samples. A sample of wrought (heavily worked by both hot and cold forging) 304L stainless steel was also prepared to serve as a baseline for comparison of the TEM results. A dual-jet electropolisher with an applied voltage of 21.5 V was used to thin each disc to electron transparency. The electrolyte was a solution of 10 pct perchloric acid and 90 pct methanol, cooled to 228 K.

An FEI Helios 600 focused ion beam (FIB) was used to prepare TEM foils to examine nanoscale surface particles from individual powder granules. As traditional methods of FIB-based TEM foil preparation call for a protective layer of Pt of C material which would encase the particles of interest and make imaging impossible, a modified FIB technique was developed. No protective layer was deposited, and the foil itself was left thicker such that surface particles would not be modified in any way by FIB preparation. The small surface particles could then be imaged in profile (tangential to the initial powder surface), allowing similar TEM analyses as conventional foils. The FIB was also used to prepare serial sections of a powder particle to examine internal porosity by milling away the particle in several large steps to observe defects.

An FEI Tecnai TF30 TEM with an accelerating voltage of 300 kV was used for imaging. The microscope was equipped with an EDAX energy dispersive spectroscopy (EDS) detector, which was used to measure elemental composition of phases. Dislocation density was measured using the dislocation end point per area method, described in detail elsewhere.[16] Particle size distributions were compiled by measuring the particle diameters for many particles using the ImageJ software package.

III. RESULTS & DISCUSSION

A. *Initial Microstructure*

The initial microstructure of the as-built and heat-treated 316L stainless steel is shown in Figures 1(a) and 1(b), respectively. These inverse pole figure (IPF) maps show the orientations and morphologies of the grains in the AM samples. Both scans were from similar areas of the build in relation to both the final part and the initial substrate. Areas scanned were near the bottom of the build. Several scans were done with a range of sample areas, locations, and step sizes to characterize the microstructure. The IPFs shown in Figure 1 are representative of the overall microstructure. The scans shown here were collected with a large area-of-interest and a step size of 5 μm. The as-built microstructure shows the typical macroscopic squamous or "fish scale" motifs common in as-built AM parts when viewing parallel to the laser travel direction. The heat-treated 316L sample recrystallized into a more

equiaxed grain structure. Figure 2 shows microtexture plots measured from EBSD. A modest decrease in overall texture is observed as a result of heat-treatment, consistent with previous work.[5] The heat-treatment was selected to produce not only this more general, equiaxed microstructure, but to dissolve and redistribute any non-equilibrium second-phase particles that may have been present in the as-built condition as a result of the AM process.

B. *Mechanical Testing*

Quasi-static mechanical tests were performed on 316L tensile specimens. The tensile data itself will be presented elsewhere, but example stress-strain curves for tensile specimens in the as-built and heat-treated conditions are shown in Figure 3. Here, the tensile direction was parallel to the build direction. The fracture surfaces from these tests, shown in Figure 4, display some unique features that are not observed in tests of non-AM specimens. Despite differences in microstructure, both fracture surfaces exhibit ductile dimpling, typical during failure of ductile metals. Interestingly, small, sub-micron sized particles are observed near the bottom of many dimples (see arrows in Figure 4). These particles are evident in both the as-built and heat-treated condition of the 316L, indicating that their solvus temperature is greater than that used for the heat-treatment, 1060 °C. The very fine size of these particles, and their location at the bottom of dimples, made energy dispersive spectroscopy (EDS) analysis prohibitively difficult using SEM. Instead, TEM was used to characterize the microstructure and determine the chemistry and morphology of such particles. Additionally, TEM was used to examine how prevalent the particles are and whether they are distributed evenly, or tend to segregate to any specific microstructural areas (such as grain boundaries).

C. *TEM Results*

Scanning transmission electron microscopy (STEM) is used throughout this work. The convergent beam creates a fine probe size, which is not only useful for selecting small areas of interest for EDS, but creates favorable imaging conditions over large areas of the sample despite large dislocation densities or local lattice distortions due to internal stresses.[16,17] Chemical composition of each material, including both the matrix and second-phase particles, was determined using EDS with a standardless quantification analysis. Consequently, the results should be treated in a somewhat qualitative fashion, as the measurement error can be significant in some cases. Several similar regions of interest were used in this work to capture a more statistically significant representation. Small local variations in chemistry at the microstructural level are expected due to the solidification process. Additionally, because the STEM probe can excite the entire thickness of the foil, particles which were overhanging the center hole in the TEM foil were preferred for analysis, as this greatly reduces the possibility of measuring matrix material above or below
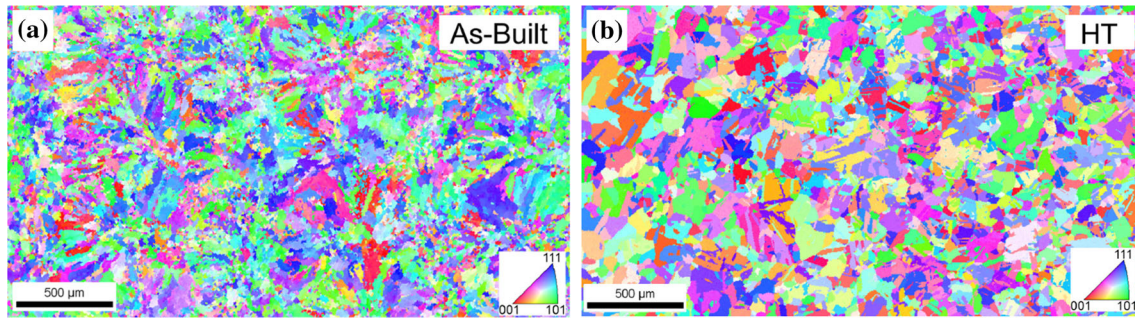
Fig. 1—Inverse pole figures for 316L stainless steel, (a) as-built condition and (b) after heat-treating at 1060°C for 1 h. Build direction is left to right in both subfigures (Color figure online).
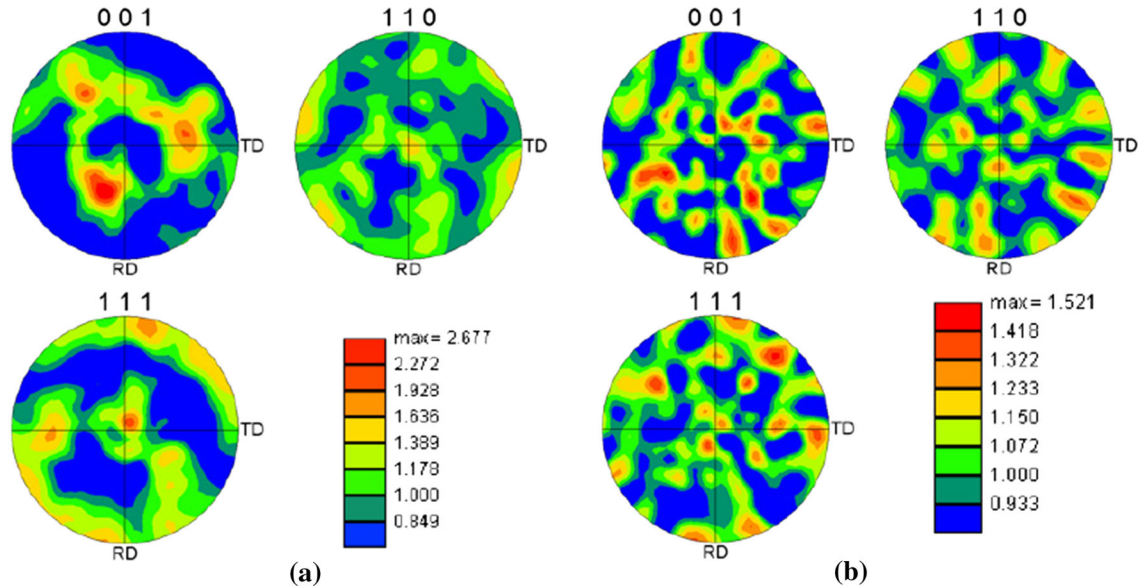

Fig. 2—Microtexture plots for 316L stainless steel, (a) as-built condition and (b) after heat-treating at 1060°C for 1 h (Color figure online).
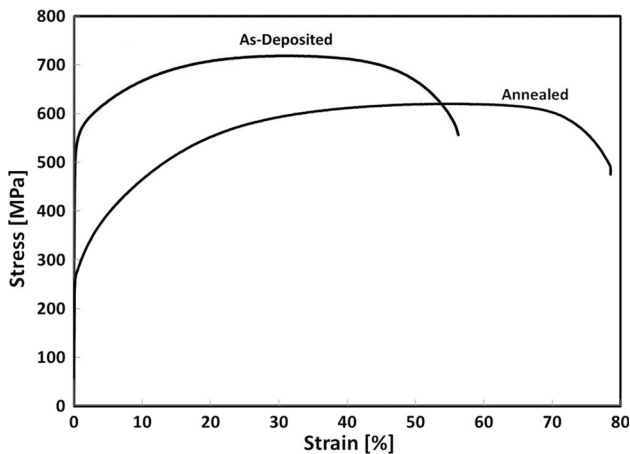

Fig. 3—Stress-strain response of AM 316L stainless steel in both the as-built and heat-treated conditions. Tensile axis is parallel to the build direction.

the particle, which would then be averaged into the EDS results.

1. 316L stainless steel

Figure 5 shows the microstructure of the 316L stainless steel produced by LENS in the as-built condition. A fine dispersion of particles were observed throughout the microstructure, consistent in size and distribution with those observed in the dimples on the fracture surfaces. Figure 6(a) shows the particle size distribution for the as-built 316L LENS build. Average particle size was 143.7 nm, with a standard deviation of 56.7 nm. There is a large spike between ~ 200 and 220 nm, representing a large population of particles near that size, more than what would be predicted by a lognormal distribution alone. Figure 6(b) shows the particle size distribution for the heat-treated 316L LENS build. Average particle size was 147.8 nm, with a standard deviation of 66.9 nm. The distribution of particles in the heat-treated specimen does not show large changes from the as-built
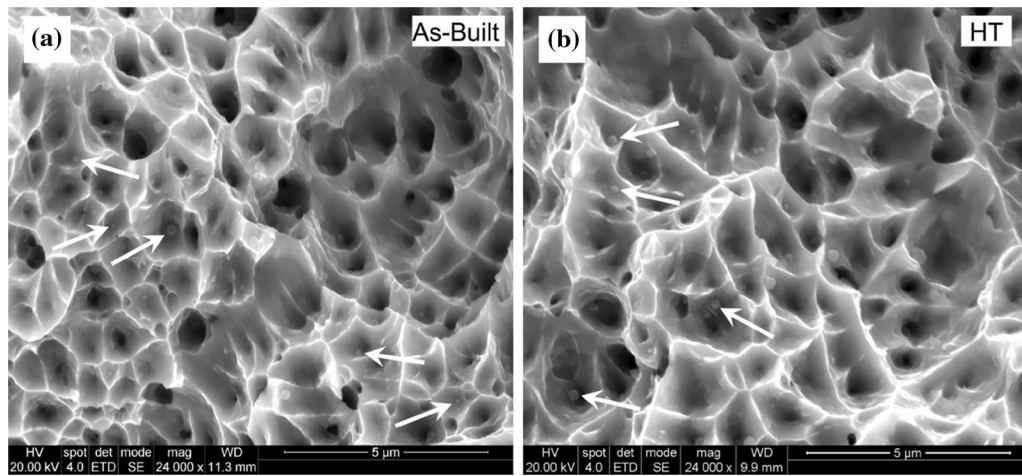
Fig. 4—Fracture surfaces for 316L stainless steel pulled in tension to failure, (*a*) as-built condition and (*b*) after heat-treating at 1060 °C for 1 h. Arrows mark a few of the many examples of fine particles observed resting inside ductile dimples throughout the fracture surface.
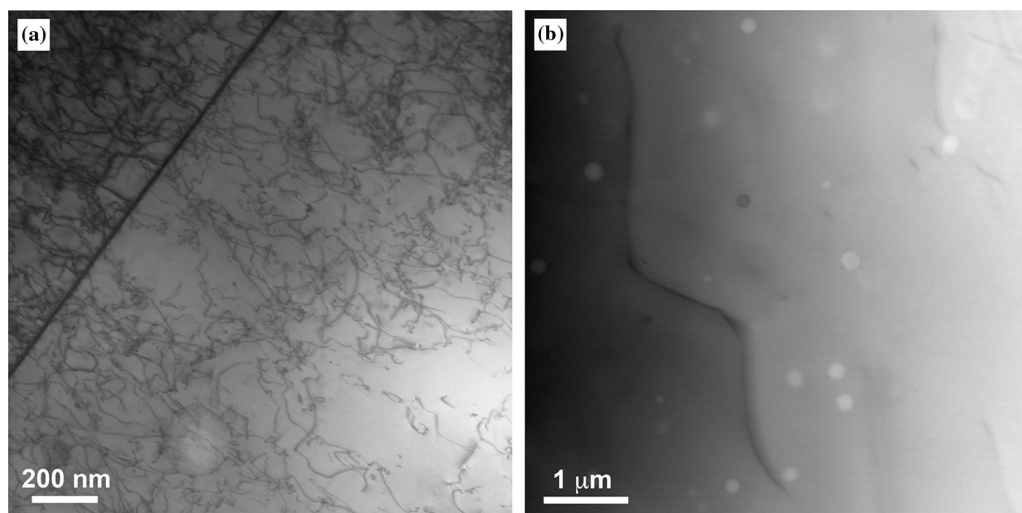

Fig. 5—(*a*) Bright-field STEM micrograph of 316L stainless steel LENS build (as-built) showing dislocations and (*b*) dark-field micrograph showing fine dispersion of sub-micron-sized particles (note: dislocations are mostly out of contrast in this image).

condition, indicating that the heat-treatment (1060 °C for 1 hr) had little effect on the particles.

One example of a particle suitable for EDS quantification is shown in Figure 7, and the resulting chemical quantification is shown in Table II. The particles often exhibited subtle faceting (as seen in Figure 7), with an apparent angle of ~ 140 deg commonly seen between adjacent faces. While the exact chemical composition varied slightly from particle to particle, the members of the class of particle of similar size and morphology as depicted in Figure 7 tended to be rich in Mn, Si, and O, and incredibly lean (relative to the nominal alloy composition) in Fe, Cr, Mo, and Ni. This composition does not resemble any of the expected second-phase compositions for 316L steel. EDS is good for qualitative measurements, but has some inherent measurement error, sometimes causing the elemental quantification to not balance to 100 pct (as is the case in Table II). Even so, larger trends and compositional differences on

the order of a few percent or larger, such as those seen for the particles measured in the as-built part, are significant relative to the experimental error reported in Table II.

Additionally, some structure within the particles was sometimes observed (manifesting as features or large deviations in contrast relative to the particle average, as in Figures 7 or 9(c)), which may be a result of thickness variations in the particles or surrounding matrix, possibly due to faceting. It is also possible that the particles adopt a more complex core-shell structure, which would also lead to different elemental composition at various parts of the particle itself. EDS performed as part of this study employed a point scan technique, and benchmarks only against matrix compositions. Details of the localized chemistry differences in particles relative to particle structure will be the subject of future work. Figure 8 shows an example of a particle in the heat-treated 316L material. Table II displays chemistry for the particles
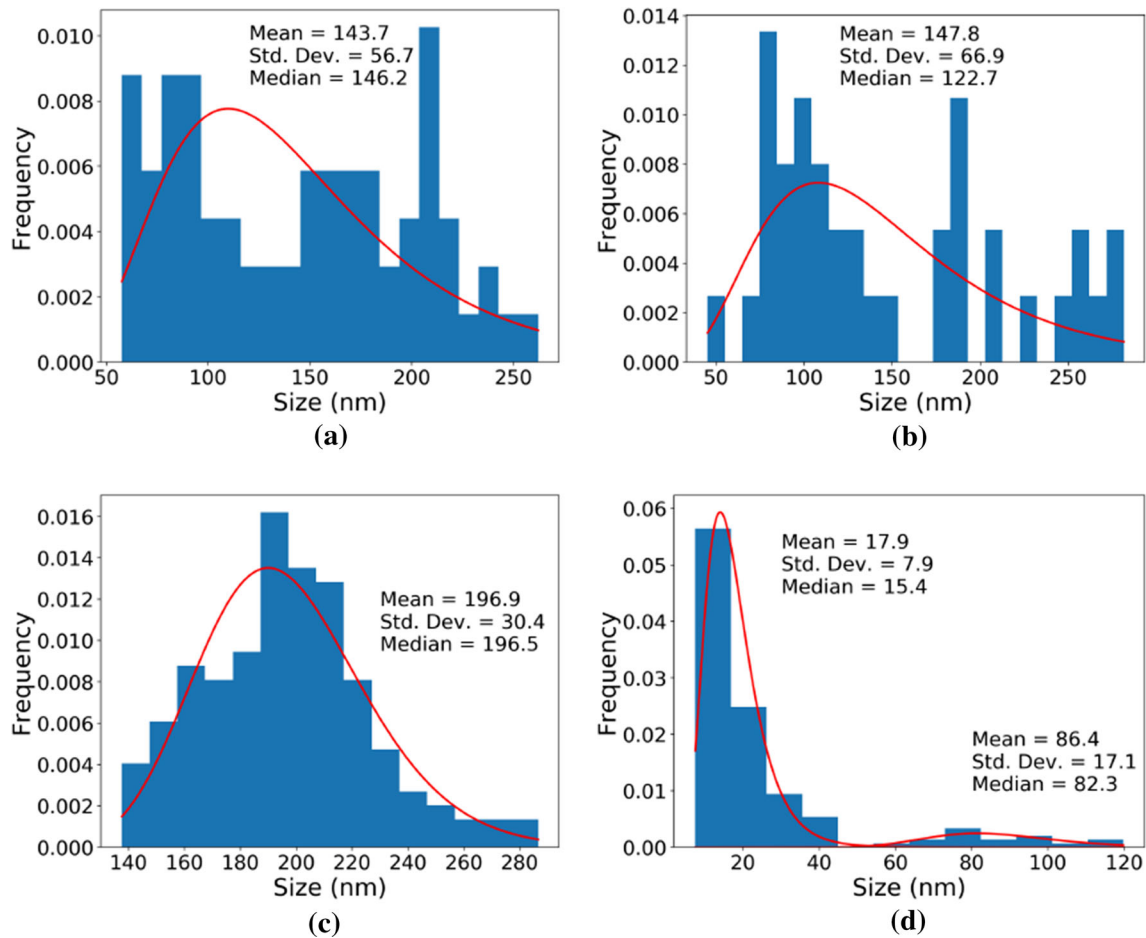
Fig. 6—Histograms of particle size distributions in AM materials: (*a*) 316L LENS build (as-built), (*b*) 316L LENS build (heat-treated), (*c*) 304L LENS build, and (*d*) 304L EOS build. The red line over each distribution represents a lognormal fit of the data (Color figure online).
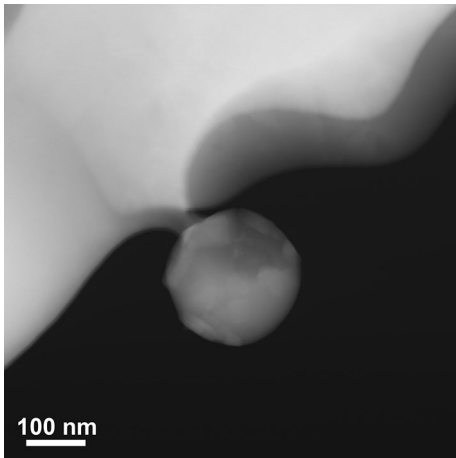

Fig. 7—Dark-field STEM image of a particle overhanging hole (dark region) in a 316L stainless steel material (LENS, as-built), tested with EDS to determine approximate chemistry.
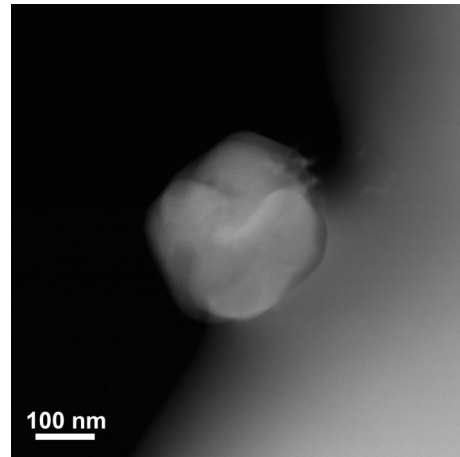

Fig. 8—Dark-field STEM image of a particle overhanging hole (dark region) in a 316L stainless steel material (LENS, heat treated at 1060 °C for 1 h), tested with EDS to determine approximate chemistry.

observed in the heat-treated 316L AM parts (as well as a summary comparison of all EDS quantifications from bulk samples in this work). As was the case for the as-built condition, the heat-treated particles are rich in Mn and O. In contrast to the as-built, however, the

heat-treated particles are also rich in Cr, and lean in Si. The mechanism for the differences in Cr and Si content due to heat-treatment is unclear. If a core-shell chemistry distribution is assumed instead of a homogeneous
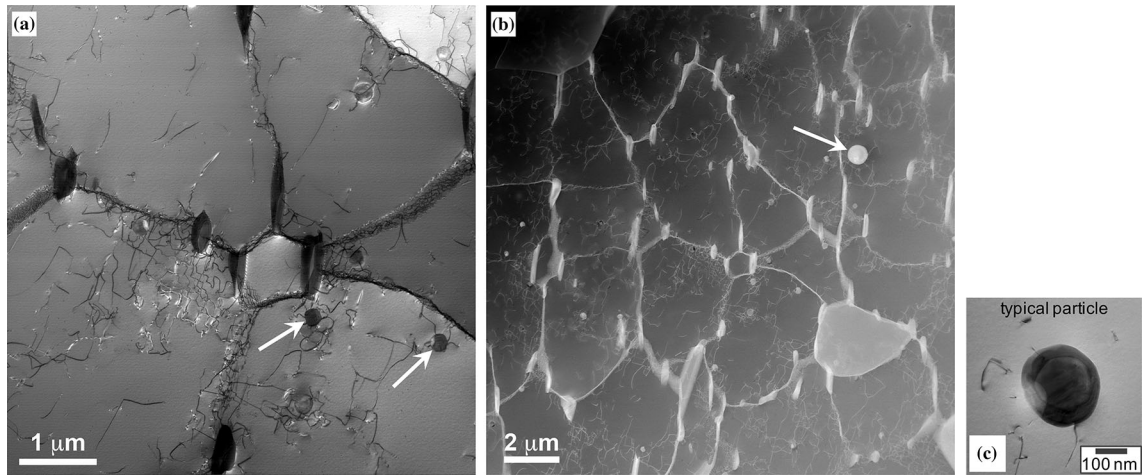
Fig. 9—(*a*) Bright-field and (*b*) dark-field STEM microstructures of 304L stainless steel LENS build showing fine dispersion of sub-micron sized particles, and (*c*) a typical particle. The arrows in (a) show examples of the fine particles found throughout the microstructure (shown larger in (c)). The arrow in (b) shows a large impurity, which are much less common though still present in the microstructure.
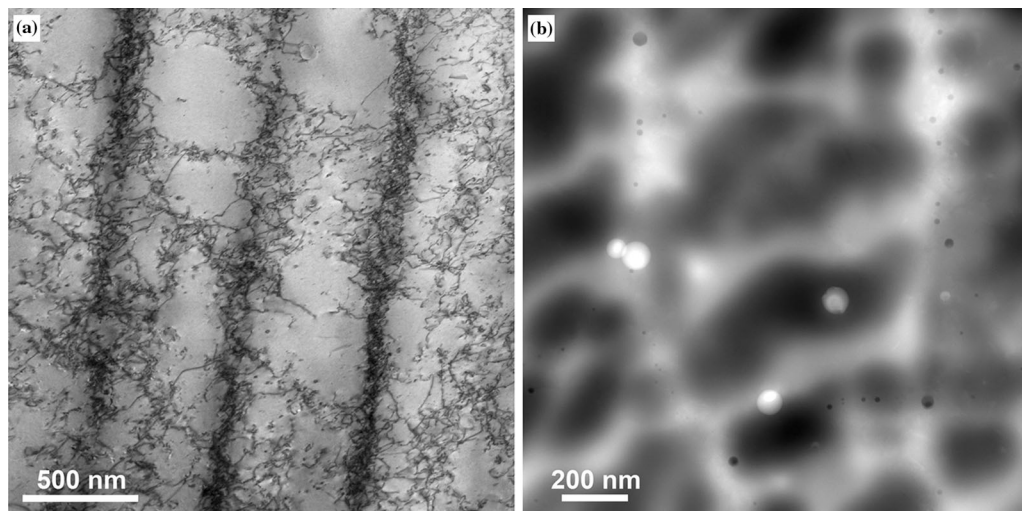

Fig. 10—(*a*) Bright-field and (*b*) dark-field STEM microstructures of 304L stainless steel EOS build showing fine dispersion of sub-micron-sized particles.

distribution, it may imply that the nuclei of such particles are stable at temperature, but that the outer shell is not. It is possible that the heat-treatment modifies only the outer shell, depleting Si while allowing a Cr shell to replace it. Alternatively, it may also be possible that the particles are formed through a separate mechanism of dissolution and reformation. However, the selected temperature was likely too low to have a large impact on oxides in the microstructure, and the fact that the size and distribution of particles are roughly the same suggests a more subtle refinement of existing particles rather than a dissolution/precipitation mechanism. Saeidi *et al.* observed particles with some qualitative similarities in 316L steel produced by laser melting in an EOS machine and subsequent heat-treatment.[18,19] Direct comparison with that work, however, is difficult. The EDS maps presented there show qualitative agreement with the deficiency in Fe, Mo, and Ni noted here. However, the authors do not report
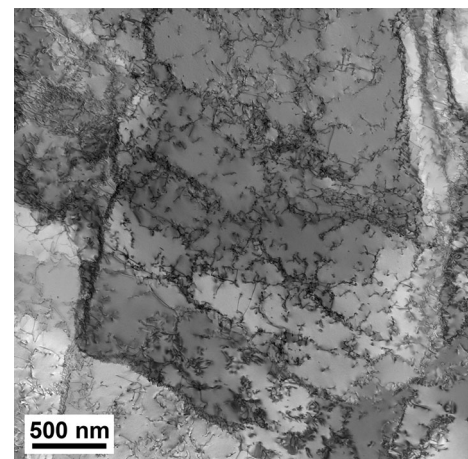

Fig. 11—Bright-field STEM micrograph of 304L stainless steel produced through a traditional wrought processing technique. No fine dispersion of particles is evident.
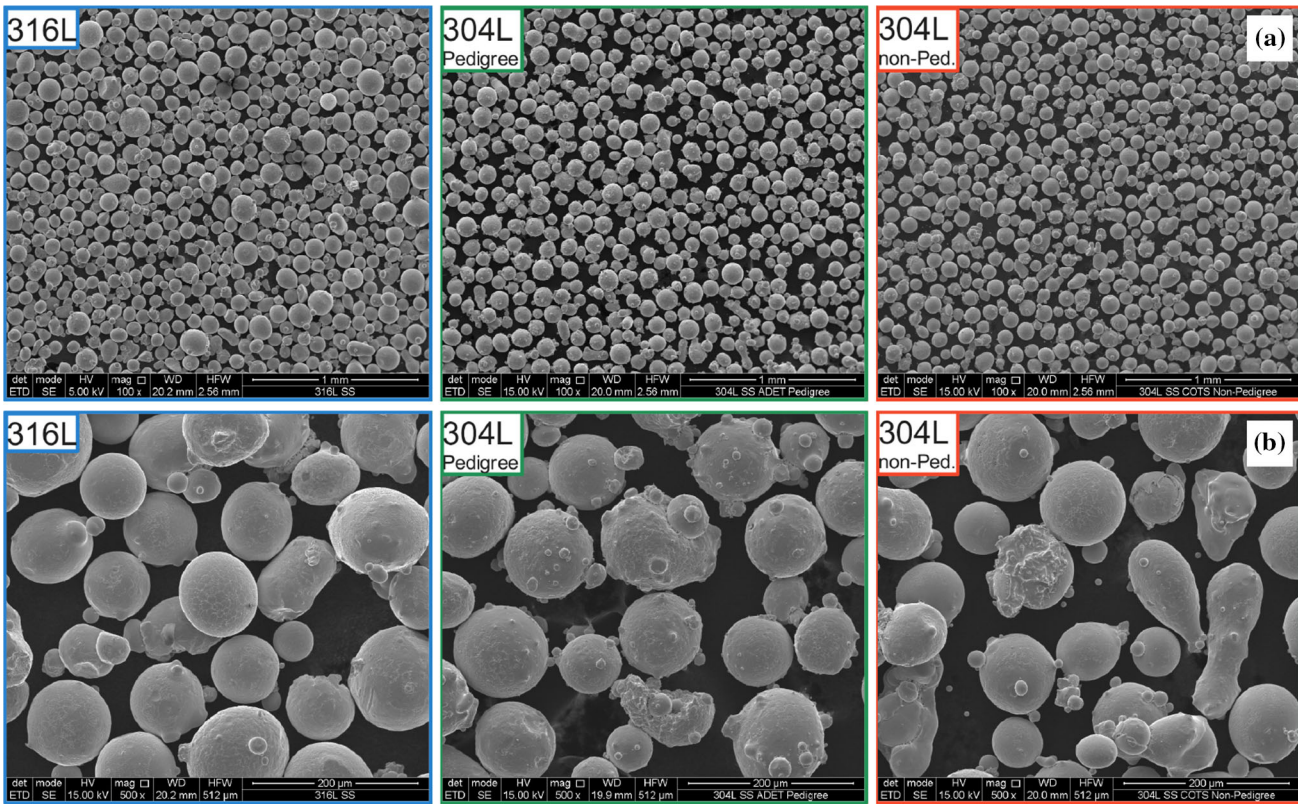
Fig. 12—SEM micrographs of representative samples of powder being studied taken at (*a*) low magnification and (*b*) higher magnification (Color figure online).
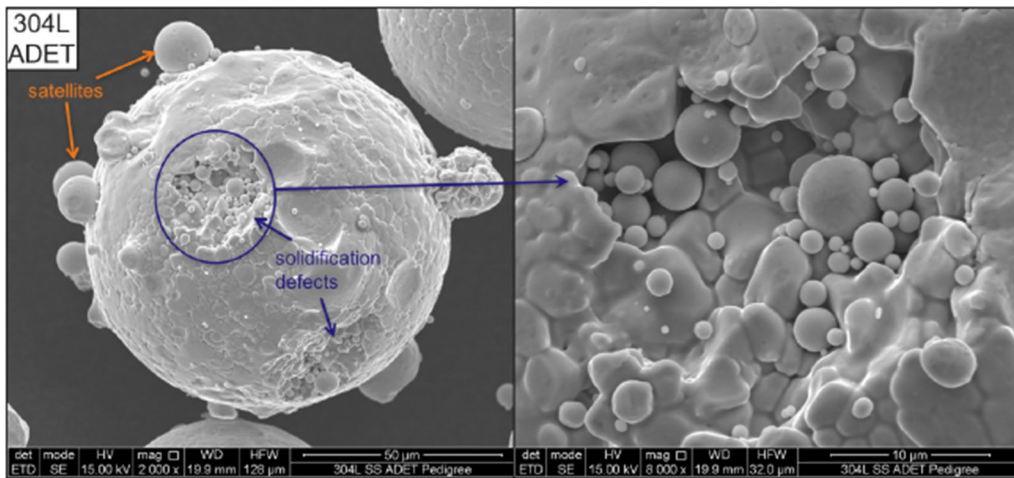

Fig. 13—SEM image of 304L stainless steel powder showing small satellites and surface defects (Color figure online).

Mn content, and the EDS map presented shows a deficiency of Cr in the particles shown, in contrast to the trend observed here (though the text indicates that the particles contain Cr, in apparent agreement with that presented here). No quantification of elemental composition of the particles was presented to compare to the present work.

Dislocation density for the as-built 316L, measured directly using the technique described above, was 2.77 $\times 10^{14}$ m^{-2} for the area shown in Figure 5(a). Very few dislocations were observed in the AM 316L steel in the

heat-treated condition, so dislocation density for that sample is not reported here. These values are in line with expectations due to the high residual stresses found in as-built AM parts, relative to a heat-treated condition. Dislocation densities for all materials in this study, measured from the micrographs presented, are shown in Table III. It should be noted that dislocation density was only quantified from the area shown in the presented micrographs. Some variability in dislocation density is to be expected in any specimen, but this variability may be especially acute when considering the
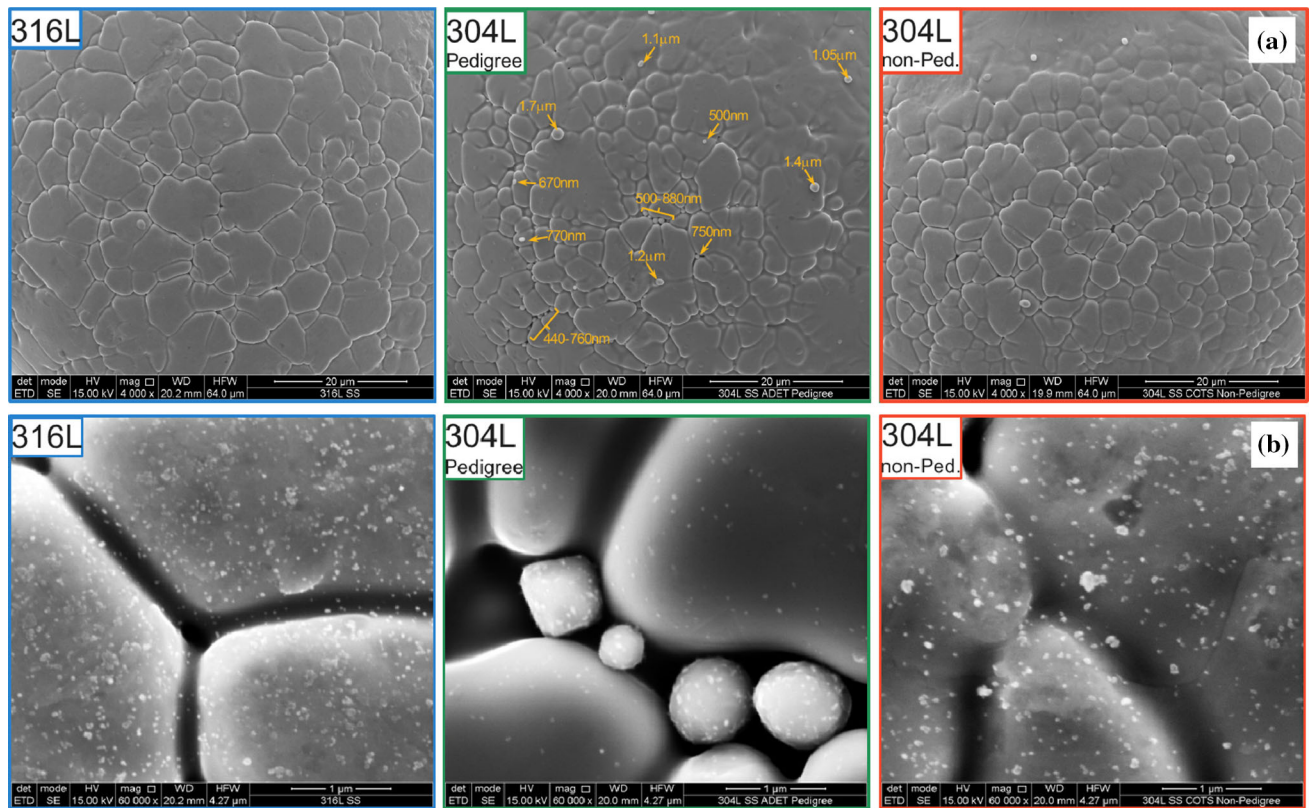
Fig. 14—SEM micrographs of representative samples of powder being studied. (*a*) The surface of the powder particles shows the dendritic structure from solidification during gas atomization. (*b*) At higher magnification, small particles are evident on the surface of each particle, seen here as bright with respect to background (Color figure online).

microstructures of as-built AM samples, which are not expected to have homogeneous distributions due to the complex solidification process and varied thermal histories.[5] Even so, qualitative comparisons may be made, and large differences in dislocation density are observed as a result of thermal history. Alloying effects are not specifically accounted for here, so comparisons between 316L and 304L materials will not be made.

2. *304L stainless steel*

Further TEM studies were performed to determine the frequency of these particles in the microstructure as a function of AM processing platform, as the LENS and EOS systems use very different processing parameters to arrive at final parts. Figure 9 shows TEM micrographs of 304L stainless steel produced by LENS. Figure 9(a) shows a bright-field micrograph of the microstructure. Regions of ferrite are visible decorating the grain boundaries. Total ferrite fraction was quantified to be < 3 pct. A dispersion of small particles of similar size and shape to those observed in the ductile dimples of the 316L fracture surfaces can be seen throughout the microstructure (two such particles are denoted by arrows in Figure 9(a)). Occasionally, very large (several hundreds of nm in diameter) particles were observed (such as the one shown by an arrow in Figure 9(b), ~775 nm). The large particle shown was rich in Si, Mn, Ca, and O, and may represent a foreign particle of soil or mineral sand, possibly originating in the feedstock

and persisting as an inclusion in the final build. Such particles, though occasionally present, are rare in the microstructure. EDS quantification for particles of similar morphology to those shown in Figure 9(a) is presented in Table II. Similar to the 316L LENS part (as-built), particles are rich in Mn, Si, and O, and lean in Fe, Cr, and Ni.

As before, dislocations are present throughout the microstructure. Dislocation density was measured at 7.45×10^{12} m^{-2} and 4.31×10^{12} m^{-2} for the area shown in Figures 9(a) and (b), respectively. This represents a moderate dislocation density, as might be expected in the as-built condition, where residual stresses are expected to be high. Furthermore, dislocations can be seen accumulating around particles in the microstructure, indicating that the particles probably contribute to hardening during plastic deformation.

Figure 10 shows STEM micrographs of the 304L EOS parts in the as-built condition. A high dislocation density was observed, (2.72×10^{14} m^{-2} for the area shown in Figure 10(a)). This is higher than the LENS built microstructure, and consistent with the lower heat input during building, faster local cooling rates, and higher residual stresses of the EOS technique. The particles observed in the microstructure were generally round in shape. Table II shows the chemistry for one such particle, though others were tested to have a similar composition. The particles are rich in Mn, Si, and O, and lean in Fe, Cr, and Ni, with respect to the nominal
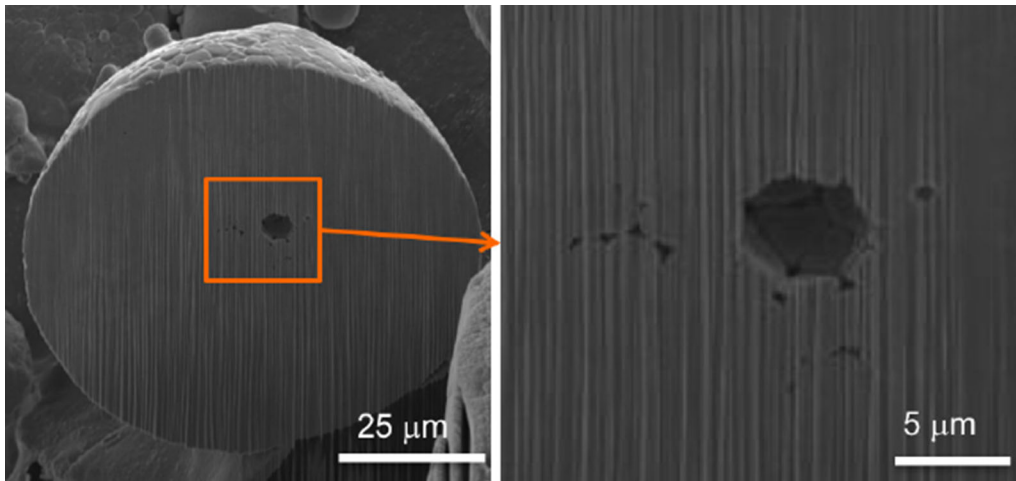
Fig. 15—SEM image of 304L stainless steel powder showing internal porosity revealed by serial sectioning (Color figure online).
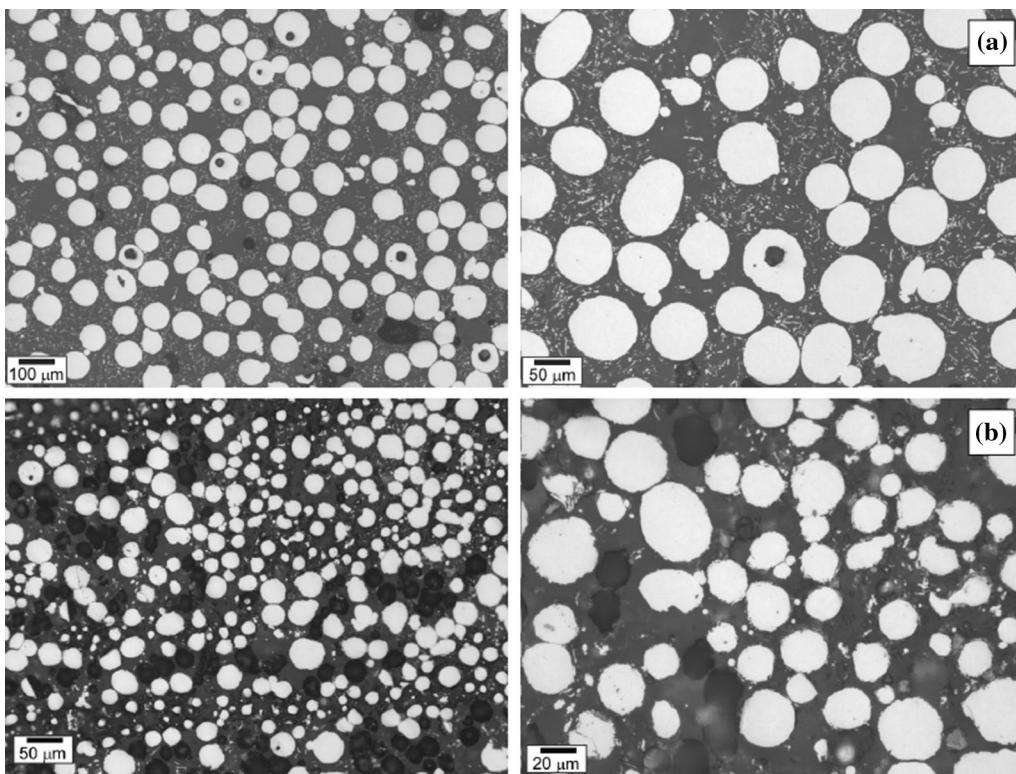

Fig. 16—Micrographs of a cross section taken through a distribution of AM powder particles for (*a*) 304L LENS powder and (*b*) 304L EOS powder. Voids are evident in each, with smaller voids apparent in the EOS powder, commensurate with their smaller size.

matrix composition. The 304L LENS built parts have a very similar composition (see Table II).

As seen in Figures 9(c) and 10, the particles in the microstructure of the 304L EOS build often display a morphology that is mostly round with ''notches'' removed from one or more areas around the outer edge of the particle. The different contrast in these notched regions indicates a decrease in material density, and line scans through the particles indicate that there might be a small preference for Si to segregate to these regions.

With greater time at temperature (such as the LENS process, or being subjected to a post-build heat-treatment), this may develop into a more consistent core–shell structure. Future work should study the internal chemistry of the particles in greater detail to examine this hypothesis.

Figure 6 shows the particle size distribution for the AM specimens. The data for the 304L LENS build are shown in Figure 6(c). Average particle size was 196.9 nm, with a standard deviation of 30.4 nm. A
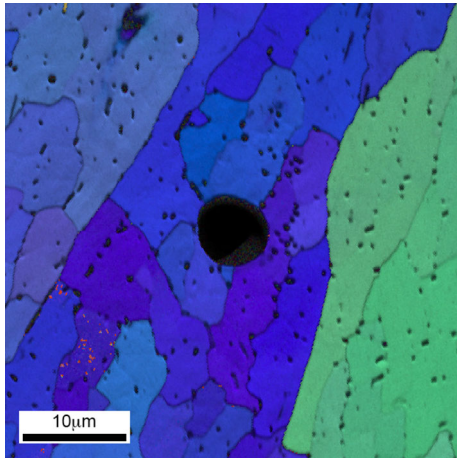
Fig. 17—IPF of an AM 304L stainless steel material (EOS, as-built) showing a large, spherical pore in the center. Such pores may originate from entrapped gas in the initial powder feedstock (Color figure online).

lognormal distribution (represented by the red line) fits the data well. Figure 6(d) shows the distribution of the 304L EOS build. Average particle size was 24.8 nm, with a standard deviation of 22.6 nm. The median for this distribution was 16.2 nm. In contrast to the LENS build, the particles in the EOS build exhibit a bimodal distribution. Most particles are very small (< 30 nm). However, there is a population of much larger particles (60 to 120 nm) present in the microstructure as well. It is important to note that overall, the particles are much smaller than for the LENS build. Assuming coarsening occurs, this smaller particle size is expected due to the much higher cooling rates operative in the EOS process leading to a reduced dwell time in the liquid phase. When accounting for these populations separately, the mean, median, and standard deviation for the small particles are 17.9, 15.4, and 7.8 nm, respectively. The mean, median, and standard deviation for the larger particles are 86.4, 82.2, and 17.1 nm, respectively.

Figure 11 shows a TEM micrograph of the wrought 304L material (not produced by additive manufacturing). The material exhibits a high dislocation density ($\sim 1.84 \times 10^{14}$ m^{-2} for the area shown), as might be expected from a wrought forged process, and similar to the EOS process. In contrast to the EOS-built material, this high dislocation density is believed to result from extensive cold-work rather than residual stresses, though the final dislocation density is similar. In contrast to the AM parts, no small Mn/Si/O-rich particles are present in the wrought material, nor were they observed in TEM studies of fusion welded 304 material,[20,21] indicating that the particles are likely a result of some step in the AM lifecycle. This is not to say that they must be due to the build itself, however, as it is also possible that the particles originate earlier in the AM lifecycle. Similar small particles were observed in each of the AM parts, regardless of process (LENS vs. EOS), or heat-treatment, as indicated in Figures 7, 9, and 10. Size distributions change somewhat, as a function of AM process parameters, but the particles are still present. Accordingly, a review of the feedstock materials was undertaken to determine which defects, if any, are present in the initial powder feedstocks, and determine how they evolve as a function of AM processing.

D. Analysis of Feedstock Material

The powder feedstock was analyzed to determine the nature and relative number of defects that may have been present before AM processing was performed. Figure 12 shows the powder used in this study. The shape and oblateness of the powders, while potentially important for flowability of the powder,[22] is beyond the scope of the present work, aside from the observation that most particles are qualitatively roughly spherical and sometimes have smaller powder particles (satellites) agglomerating on the surface of larger particles. An example of this is shown in Figure 13. Additionally, solidification defects are sometimes found on the surface (also shown in Figure 13), characterized by regions of relative disorder at the powder surface, sometimes filled with smaller nodules of material. Such defects may increase surface roughness, but are not expected to markedly affect the AM build process. A closer look at the typical powder surface (Figure 14) shows a mostly smooth surface, with evidence of solidification structure. At the highest magnifications, a fine dispersion of particles can be noted. These particles are typically on the order of 30-60 nm, making in situ chemical analysis extremely difficult in SEM. Hence, to measure surface particle chemistry in TEM, a modified focused ion beam (FIB) TEM foil extraction procedure was developed. Unlike a conventional FIB-prepared TEM foil, no Pt or C protective layer was used so as not to obscure the surface particles. To view as many particles as practical, the foil was left somewhat thick (on the order of a few microns). The features at the surface of the particle were then viewed from the side (tangential to the original surface of the particle), and were small enough to be electron transparent without additional preparation, enabling viewing with TEM where they protruded above the surface of the particle. This technique enabled limited EDS of surface particles similar to those previously performed. EDS spot analysis for the powder is shown in Table IV. The chemistry of the bulk (sub-surface regions) of the powder are similar to the expected values from Table I. EDS analyses for two different surface regions are also shown in Table IV, representative of several different measurements. All of the surface particle scans showed below-nominal levels of Cr. One surface particle was rich in Mn and Ni, while the other was lean. The second surface particle scan also showed significant O content. Both particles shown in Table IV show greatly increased Si content compared to bulk. Recall that the particles observed in as-built 316L and 304L parts were lean in Cr, while rich in Mn, Si, and O. This strongly suggests that the surface particles of the powder contribute or directly translate to the particles observed in the final parts shown in this work. Overall, a significant amount of variability in chemistry was observed between surface particles. This could be a result of the powder production process, and suggests that the starting powders are not chemically

Table II. Summary of EDS Quantification of Particles from the AM Builds (Weight Percent)

Element	316L AB	316L HT	304L LENS	304L EOS
Fe	2.7 ± 0.1	0.0	3.6 ± 0.1	2.8 ± 0.4
Cr	6.4 ± 0.3	39.1 ± 0.2	4.4 ± 0.1	9.8 ± 4.5
Mn	16.6 ± 0.4	27.0 ± 0.1	30.1 ± 0.2	5.7 ± 0.5
O	36.6 ± 0.8	28.5 ± 0.4	36.6 ± 0.3	34.9 ± 3.3
Si	31.4 ± 0.5	0.0	23.1 ± 0.2	46.5 ± 1.1
Mo	0.6 ± 0.2	0.0	0.0	0.0
Ni	0.0	0.0	0.01 ± 0.01	0.1 ± 0.2

Measurements correspond to as-built 316L LENS particle (Fig. 7), heat-treated 316L LENS particle (Fig. 8), as-built 304L LENS particle, and as-built 304L EOS particle.

Table III. Measured Dislocation Density for the Microstructural Areas Shown in Micrographs of AM and Wrought 304L and 316L Stainless Steels Shown in Figs. 5, 9, 10, and 11

Material	Dislocation density (m^{-2})
316L LENS HT	too low to quantify
316L LENS AB	2.77×10^{14} m^{-2}
304L LENS AB	4.31 to 7.45×10^{12} m^{-2}
304L EOS AB	2.72×10^{14} m^{-2}
304L Wrought	1.84×10^{14} m^{-2}

Table IV. EDS Quantification of Surface Particles from a 316L Powder Granule (Weight Percent)

Element	Powder Bulk	Surface 1	Surface 2
Cr	20.7	5.5	9.4
Mn	2.9	4.6	0.01
O	—	0.0	19.5
Si	0.6	24.8	24.0
Mo	3.2	0.7	1.4
Ni	8.0	30.6	6.9
Fe	balance	balance	balance

homogeneous initially. This might be expected from a rapid solidification process like gas atomization. Additionally, occasionally surface particles were seen to have somewhat elevated levels of P or S, both seen in trace amounts in the bulk material and as-built parts. If these elements segregate to the surfaces of the powder, they must disperse during subsequent processing, as these elements were not seen outside the expected range previously. A systematic study of initial powder chemistry would be beneficial in future studies. It should be noted that, although not pictured in Figure 13, these particles are also present on the EOS powder, as well, at roughly the same scale, indicating that the powders probably originate from the same or similar process and are sieved to select the appropriate size for each AM process. Additionally, the particles are present in both the ADET and COTS 304L powder, suggesting that the small difference in chemistry had no marked effect on

surface particle formation. It is not definitively known whether these particles are confined to the surfaces of the powder, or if there is also a population internal to the powder, though no internal particles were obvious in the cross sections discussed below. The very fine size of these particles is much smaller than the particles observed during TEM of the AM parts, indicating that if these are precursors to those observed in the AM microstructures, they must coarsen during the AM build process (and any subsequent heat-treatment).

Internal porosity is a common defect in parts built using AM. Often, these are assumed to arise from a lack of fill or fusion, or incomplete powder melting, due to insufficient heat input. Due to rapid cooling rates and fast solidification rates inherent to AM, porosity internal to the powder feedstock has the potential to be incorporated directly into the final parts, as well. To investigate this, a single granule of 304L stainless steel powder was serial sectioned in a FIB to determine whether voids exist inside a particle that otherwise appeared defect-free. Figure 15 shows one of the several sections taken through a particle. It should be noted that the vertical striations present in the images are a curtaining artifact from the FIB, a result of slightly uneven ion milling due to the large particle size and lack of a protective Pt deposited on top of the particle, and do not affect the observed voids. Porosity is evident throughout the particle, but the largest cavities tend to be near the center of the powder. Additionally, many of the pores have a faceted structure, consistent with solidification defects. Because the powders were created through a gas atomization process, it is most probable that the powders have some content of entrapped gas, which, when cooling rates are considered, is likely to also be directly incorporated and present in the final microstructures of AM parts. The FIB technique is useful to obtain a view of internal porosity at many depths in a single particle. To increase statistics over many particles, a single section technique is used, wherein each powder was embedded in epoxy and prepared metallographically such that a cross section through many particles could be viewed. Figure 16 shows these cross sections for both LENS and EOS 304L stainless steel powder. Similar to the serial sectioning, many particles contain large pores near the center of the powder granules. Some are a significant fraction of the overall particle diameter. Most particles contain at least some small pores, though the smaller sized pores may not substantially impact final build quality. It is likely that final pore population (size and distribution) in as-built AM parts depends not only on the initial pore population found in the feedstock materials, but also the processing parameters of the AM build process itself. This is consistent with the findings of Ng et al.,[12] who observed similar behavior in gas atomized Inconel 718. An in-depth discussion on gas entrapment as a function of processing (and specifically Marangoni flow) can be found there.

Cooling rate, specifically, is expected to have a large impact on final pore sizes. Hofmeister et al. measured cooling rates at the solid-liquid interface for the LENS

process on the order of 10^2 to 10^3 K s^{-1} depending on processing conditions.[23] This is more or less consistent with cooling rates numerically calculated[24] and experimentally determined[25] by Zheng *et al.*, where rates were found to be as high as 10^3 to 10^4 K s^{-1}. Gray *et al.*[9] calculated cooling rates of 5.5×10^3 to 1.1×10^4 Ks^{-1} in the same LENS-produced 316L stainless steel used in this study by measuring interdendritic spacing.[26] Applying this same technique here for EOS-produced 304L (using the same parameters presented in Reference 9) yields a cooling rate of $\sim 2.25 \times 10^6$ Ks^{-1} (for the area shown in Figure 10. Vilaro *et al.* have estimated a cooling rate of $\sim 10^4$ K s^{-1} for powder bed techniques.[27] Vilaro also noted entrapped gas in as-built parts, but attributed them to gas trapped between particles of powder. These cooling rates are sufficiently fast that gas trapped in powder particles may not escape before solidification. Given the large pores shown in Figure 15, gas internal to the powder feedstock particles should also be considered as a point of origin for such entrapped gas.

Figure 17 shows an EBSD IPF map of 304L stainless steel in the as-built condition, with a large spherical pore clearly visible in the center of the image. It is also notable that this pore occurs internal to a single grain, not at a grain boundary as would be expected from a lack-of-fusion or solidification defect.

This is consistent with similar porosity defects in Ti-6Al-4V.[13,28] Cunningham et al quantitatively observed pore populations in as-built Ti-6Al-4V material using X-ray tomography.[13–15] Average pore size was approximately 10 μm in that work, though the resolution limit of 1.5 μm may prevent imaging the smallest pores. Certainly some of the largest pores, ~ 50 μm, could be consistent with porosity present in the powder feedstock material, as demonstrated by Figure 16. Investigation of whether there is a critical flaw size for AM parts which impacts relevant materials properties during service should be considered, but is outside the scope of the current work. It is important to note that if such pores are filled with entrapped inert gas carried over from the starting powder feedstock, a hot isostatic press (HIP) treatment, often used to attempt to close porosity due to solidification defects,[3,29] will not remove this porosity.[15]

IV. CONCLUSIONS

Additive manufacturing was used to build several 304L and 316L stainless steel parts. For the 316L material, a directed energy deposition technique was used to build parts, and a subsequent heat-treatment was applied to some of the samples. Two different processes were used, directed energy deposition and powder bed fusion, each requiring similar feedstock powder with different size distributions. Resultant fracture surfaces from tensile testing revealed ductile dimples typical of structural metals, but small precipitates were observed in many of the dimples. An examination of the microstructure using TEM revealed that the AM parts had a fine dispersion of sub-micron (< 200 nm for LENS, < 120 nm for EOS) particles throughout the microstructure. Chemistry of the particles was measured using EDS. Relative to the matrix composition, they were rich in Mn, Si, and O, and deficient in Fe, Cr, Mo, and Ni. Post-build heat-treatment had only a small effect on the precipitates. Heat-treated particles were roughly the same size as the particles in the as-built microstructure. Chemistry of the heat-treated particles was slightly different than the as-built condition: rich in Mn, O, and Cr, while lean in Fe, Mo, Ni, and Si. Such particles were neither observed in wrought material, nor reported in previous literature on fusion welding in steels, indicating that the particles are likely a function of the unique AM lifecycle.

Powder feedstock was analyzed to determine if the particles were present before the build, or if they were a result of the AM process. Very small (30 to 60 nm) particles were observed on the surface of the powder feedstock granules, thought to be a result of the powder manufacturing process. EDS was used to measure chemical composition of particles on the surface of powder granules. While overall chemistry was fairly heterogenous relative to bulk, the chemical composition at the surface particles was similar to the composition of particles in as-built parts, indicating that the two populations are correlated. Porosity, sometimes large relative to particle size, was observed as well. Gas atomization of powder feedstock raises the potential that these internal defects are filled with inert gas, which may become trapped in AM parts as bubbles due to the rapid solidification rates inherent to AM processing.

Aside from the AM-related particles, TEM was used to characterize the microstructures of AM materials. Ferrite phase was observed in parts created by LENS, but was not observed in EOS-made material. Dislocation density was quantified for all processes, including wrought material. Dislocation density was highest in wrought and EOS (which were similar), and lowest in LENS material. Very few dislocations were observed in heat-treated LENS material. This is all consistent with the respective thermal histories expected from each process.

REFERENCES

1. E.C. Santos, M. Shiomi, K. Osakada, and T. Laoui: *Int. J. Mach. Tools Manuf.*, 2006, vol. 46, pp. 1459–68.
2. W.E. Frazier: *J. Mater. Eng. Perform.*, 2014, vol. 23, pp. 1917–28.
3. A.M. Beese and B.E. Carroll: *JOM*, 2016, vol. 68, pp. 724–34.
4. G.T. Gray, III, V. Livescu, P.A. Rigg, C.P. Trujillo, C.M. Cady, S.R. Chen, J.S. Carpenter, T.J. Lienert, and S.J. Fensin: *EPJ. Web Conf.*, 2015, vol. 94, p. 02006.

5. V. Livescu, C.A. Bronkhorst, S.A. Vander Wiel, D.W. Brown, J.R. Mayeur, G.T. Gray III, J.S. Carpenter, O.F. Dippo, and M.L. Lovato: in *The Ninth Pacific Rim International Conference on Advanced Materials and Processing (PRICM9)*, M.N.T. Furuhara and S. Miura, eds., The Japan Institute of Metals and Materials, 2016 pp. 1–6.
6. J.J. Lewandowski and M. Seifi: *Annu. Rev. Mater. Res.*, 2016, vol. 46, pp. 151–86.
7. M. Seifi, A. Salem, J. Beuth, O. Harrysson, and J.J. Lewandowski: *JOM*, 2016, vol. 68, pp. 747–64.
8. M.M. Francois, A. Sun, W.E. King, N.J. Henson, D. Tourret, C.A. Bronkhorst, N.N. Carlson, C.K. Newman, T. Haut, J. Bakosi, J.W. Gibbs, V. Livescu, S.A. Vander Wiel, A.J. Clarke, M.W. Schraad, T. Blacker, H. Lim, T. Rodgers, S. Owen, F. Abdeljawad, J. Madison, A.T. Anderson, J.L. Fattebert, R.M. Ferencz, N.E. Hodge, S.A. Khairallah, and O. Walton: *Curr. Opin. Solid State Mater. Sci.*, 2017, pp. 1–9.
9. G. Gray, V. Livescu, P. Rigg, C. Trujillo, C. Cady, S. Chen, J. Carpenter, T. Lienert, and S. Fensin: *Acta Mater.*, 2017, vol. 138, pp. 140–49.
10. H. Gong, K. Rafi, H. Gu, T. Starr, and B. Stucker: *Addit. Manuf.*, 2014, vol. 1–4, pp. 87–98 (inaugural Issue).
11. H.P. Tang, M. Qian, N. Liu, X.Z. Zhang, G.Y. Yang, and J. Wang: *JOM*, 2015, vol. 67, pp. 555–63.
12. G.K.L. Ng, A.E.W. Jarfors, G. Bi, and H.Y. Zheng: *Applied Physics A*, 2009, vol. 97, p. 641.
13. R. Cunningham, S.P. Narra, T. Ozturk, J. Beuth, and A.D. Rollett: *JOM*, 2016, vol. 68, pp. 765–71.
14. R. Cunningham, S.P. Narra, C. Montgomery, J. Beuth, and A.D. Rollett: *JOM*, 2017, vol. 69, pp. 479–84.
15. R. Cunningham, A. Nicolas, J. Madsen, E. Fodran, E. Anagnostou, M.D. Sangid, and A.D. Rollett: *Mater. Res. Lett.*, 2017, vol. 5, pp. 516–25.
16. B.M. Morrow, R.W. Kozar, K.R. Anderson, and M.J. Mills: *Acta Mater.*, 2013, vol. 61, pp. 4452–60.
17. B.M. Morrow, R.W. Kozar, K.R. Anderson, and M.J. Mills: *Mater. Sci. Eng. A*, 2016, vol. 665, pp. 90–97.
18. K. Saeidi, X. Gao, F. Lofaj, L. Kvetková, and Z. Shen: *J. Alloys Compd.*, 2015, vol. 633, pp. 463–69.
19. K. Saeidi, X. Gao, Y. Zhong, and Z. Shen: *Mater. Sci. Eng. A*, 2015, vol. 625, pp. 221–29.
20. H. Kokawa, T. Kuwana, and A. Yamamoto: *Weld. J.*, 1989, vol. 68, pp. S92–S101.
21. C.-M. Lin, H.-L. Tsai, C.-D. Cheng, and C. Yang: *Eng. Fail. Anal.*, 2012, vol. 21, pp. 9–20.
22. J.A. Slotwinski and E.J. Garboczi: *JOM J. Miner. Metals Mater. Soc.*, 2015, vol. 67, pp. 538–43.
23. W. Hofmeister and M. Griffith: *JOM*, 2001, vol. 53, pp. 30–34.
24. B. Zheng, Y. Zhou, J.E. Smugeresky, J.M. Schoenung, and E.J. Lavernia: *Metall. Mater. Trans. A*, 2008, vol. 39, pp. 2228–36.
25. B. Zheng, Y. Zhou, J.E. Smugeresky, J.M. Schoenung, and E.J. Lavernia: *Metall. Mater. Trans. A*, 2008, vol. 39, pp. 2237–45.
26. M.C. Flemings: *Solidification Processing*, Wiley-VCH Verlag GmbH & Co. KGaA, Weinheim, 2006.
27. T. Vilaro, C. Colin, and J.D. Bartout: *Metall. Mater. Trans. A*, 2011, vol. 42, pp. 3190–99.
28. S. Tammas-Williams, H. Zhao, F. Léonard, F. Derguti, I. Todd, and P.B. Prangnell: *Mater. Charact.*, 2015, vol. 102, pp. 47–61.
29. S. Das, M. Wohlert, J.J. Beaman, and D.L. Bourell: *Mater. Des.*, 1999, vol. 20, pp. 115–21.